Dynamic Properties of Human α-Synuclein Related to Propensity to Amyloid Fibril Formation

Satoru Fujiwara [1], Fumiaki Kono [1], Tatsuhito Matsuo [1], Yasunobu Sugimoto [2], Tomoharu Matsumoto [3], Akihiro Narita [3] and Kaoru Shibata [4]

1 - Institute for Quantum Life Science, *National Institutes for Quantum and Radiological Science and Technology, 2-4 Shirakata, Tokai, Ibaraki 319-1106, Japan*
2 - Nagoya University Synchrotron Radiation Research Center, *Furo-cho, Chikusa-ku, Nagoya, Aichi 464-0965, Japan*
3 - Structural Biology Research Center, *Garduate School of Science, Nagoya University, Furo-cho, Chikusa-ku, Nagoya, Aichi 464-8601, Japan*
4 - Neutron Science Section, *Materials and Life Science Division, J-PARC Center, Japan Atomic Energy Agency, 2-4 Shirakata, Tokai, Ibaraki 319-1195, Japan*

Correspondence to Satoru Fujiwara: *Institute for Quantum Life Science, National Institutes for Quantum and Radiological Science and Technology, 2-4 Shirakata, Tokai, Naka-Gun, Ibaraki 319-1106, Japan.* *fujiwara.satoru@qst.go.jp*
https://doi.org/10.1016/j.jmb.2019.05.047
Edited by Louise C. Serpell

Abstract

α-Synuclein (αSyn) is an intrinsically disordered protein that can form amyloid fibrils. Fibrils of αSyn are implicated with the pathogenesis of Parkinson's disease and other synucleinopathies. Elucidating the mechanism of fibril formation of αSyn is therefore important for understanding the mechanism of the pathogenesis of these diseases. Fibril formation of αSyn is sensitive to solution conditions, suggesting that fibril formation of αSyn arises from the changes in its inherent physico-chemical properties, particularly its dynamic properties because intrinsically disordered proteins such as αSyn utilize their inherent flexibility to function. Characterizing these properties under various conditions should provide insights into the mechanism of fibril formation. Here, using the quasielastic neutron scattering and small-angle x-ray scattering techniques, we investigated the dynamic and structural properties of αSyn under the conditions, where mature fibrils are formed (pH 7.4 with a high salt concentration), where clumping of short fibrils occurs (pH 4.0), and where fibril formation is not completed (pH 7.4). The small-angle x-ray scattering measurements showed that the extended structures at pH 7.4 with a high salt concentration become compact at pH 4.0 and 7.4. The quasielastic neutron scattering measurements showed that both intra-molecular segmental motions and local motions such as side-chain motions are enhanced at pH 7.4 with a high salt concentration, compared to those at pH 7.4 without salt, whereas only the local motions are enhanced at pH 4.0. These results imply that fibril formation of αSyn requires not only the enhanced local motions but also the segmental motions such that proper inter-molecular interactions are possible.

Introduction

Parkinson's disease (PD) is the second most common neuro-degenerative disorder after Alzheimer's disease [1]. The hallmarks of this disease include loss of dopaminergic neurons in the *substantia nigra* in the brain and the formation of intracytoplasmic aggregates, called Lewy bodies, the major component of which is fibrillar aggregates (amyloid fibrils) of α-synuclein (αSyn) [2]. Missense mutations in the gene of this protein have been identified in early-onset PD [3–8]. Overexpression of αSyn due to duplication and triplication of this gene have also been shown to cause familial early-onset PD [9–11]. These observations imply that amyloid fibril formation of αSyn is involved with the pathogenesis of PD.

αSyn is an intrinsically disordered protein, containing the N-terminal (1–60 residues) and C-terminal (96–140 residues) regions that are disordered and the central NAC (non-amyloid-β component) region (61–95 residues) [12]. αSyn is abundant in presynaptic nerve cells [13], and this protein has been reported to be implicated with a variety of functions, including those related to synaptic plasticity, vesicle dynamics, and

neurotransmitter release [14]. The involvement of this protein with such numerous functions has led to the concept of "multifunctionality" of αSyn [15]. Amyloid fibrils of αSyn have been shown to be associated with not only PD but also other neurodegenerative diseases such as dementia with Lewy bodies and multiple system atrophy [1]. Elucidating the mechanism of fibril formation of αSyn is therefore important for understanding the mechanism of the pathogenesis of these synucleinopathies. αSyn has thus been the focus of extensive studies (as reviewed, for example, in Refs. [16,17]), the subjects of which include the kinetic process of fibril formation, the structural characterization in various states, the cytotoxicity of the aggregates, and the effects and possible therapeutic applications of various inhibitors of fibril formation. The molecular mechanism of fibril formation of αSyn, however, remains elusive.

Intrinsically disordered proteins contain conformational fluctuations as an inherent property, and they utilize this dynamic property for function [18]. Conformational fluctuations in intrinsically disordered αSyn are thus likely to play a role in the process of aggregation. Indeed, the measurements of the intramolecular diffusion of αSyn by Förster resonance energy transfer (FRET) [19–21], the conformational fluctuations of αSyn by NMR [22–27], and the local motions of the polypeptide side-chains of αSyn by quasielastic neutron scattering (QENS) [28,29] suggest the importance of these motions in fibril formation. Studies in terms of the dynamic properties are therefore required to elucidate the molecular mechanism of fibril formation of αSyn.

The kinetics as well as the pathway of aggregation *in vitro* is sensitive to the conditions of the solution in which αSyn is dispersed. The rate of fibril formation is changed by the concentrations and kinds of salts in the solution [30,31]. Incubation of αSyn at high temperature under constant shaking leads to the formation of fibrils at neutral pH, but to amorphous aggregates at acidic pH [32,33]. Even the fibrils formed have distinct features depending on the solution condition [34,35]. Thus, the propensity to fibril formation can be controlled by the solution condition. Characterization of the dynamic properties of αSyn under the conditions corresponding to the different propensities to fibril formation should provide clues to elucidate how the dynamic properties of αSyn are related to fibril formation. Since recent studies suggest the cytotoxicity of oligomeric intermediates [36–38], it is particularly important to elucidate how the initial process of aggregation starts. We thus investigated in this study the dynamic properties of αSyn monomers under various solution conditions showing different propensities to fibril formation, to elucidate how the (possible) dynamic changes of αSyn can start the initial process of aggregation.

We employed QENS to characterize the dynamic properties of αSyn. QENS provides a tool to directly measure the protein dynamics at pico- to nano-second time and ångstrom length scales [39]. Since the incoherent QENS signals arise primarily from hydrogen atoms, the (incoherent) QENS measurements on the protein samples in D_2O solutions provide the average spectra of the hydrogen atoms within the proteins. About half of the atoms constituting the proteins are hydrogen atoms, which are distributed (pseudo-)uniformly in the proteins, and the motions of the hydrogen atoms reflect the motions of larger groups of atoms to which the hydrogen atoms are bound [39]. QENS spectra thus provide information on the average dynamics of the entire proteins. In particular, the information on global motions such as diffusive motions of the entire protein and local motions such as those of side-chains can be obtained [40]. We carried out the QENS measurements on the αSyn solutions in D_2O under various salt and pH (pD) conditions, and characterized the dynamic properties of αSyn under these conditions.

We also characterized the structures of αSyn under these conditions as well. For this purpose, we carried out the small-angle x-ray scattering (SAXS) measurements on the αSyn solutions. SAXS is a powerful method to characterize the structures of the proteins in solution. The molecular parameters such as a radius of gyration, obtained from SAXS analysis, are sensitive to the shapes and association states of the proteins, and the sophisticated methods of analysis with modeling make it possible to analyze the structures in detail [41]. We combined the dynamic and structural information to elucidate the relationship between the dynamics and structures of αSyn related to fibril formation.

Results

Structural characterization of the aggregated states in various solution conditions

The following solution conditions showing different propensities to fibril formation were employed: The solution containing 20 mM Hepes (pH 7.4) and 150 mM NaCl (termed "pH 7.4 in high salt" below), that containing only 20 mM Hepes (pH 7.4), and that containing 20 mM sodium acetate (pH 4.0). Incubation of the αSyn solution at pH 7.4 at 37 °C with constant stirring leads to the formation of amyloid fibrils, but the rate and the degree of fibril formation are different in the presence and absence of salt. On the other hand, incubation of the solution at pH 4.0 is known to result in the formation of amorphous aggregates [32,33]. Figure 1(a) shows the aggregation kinetics under these solution conditions, monitored by the increase in the thioflavin T (ThT) fluorescence associated with the binding of the dye to the fibrils [42]. The aggregation kinetics was sensitive to the solution conditions: The αSyn solution

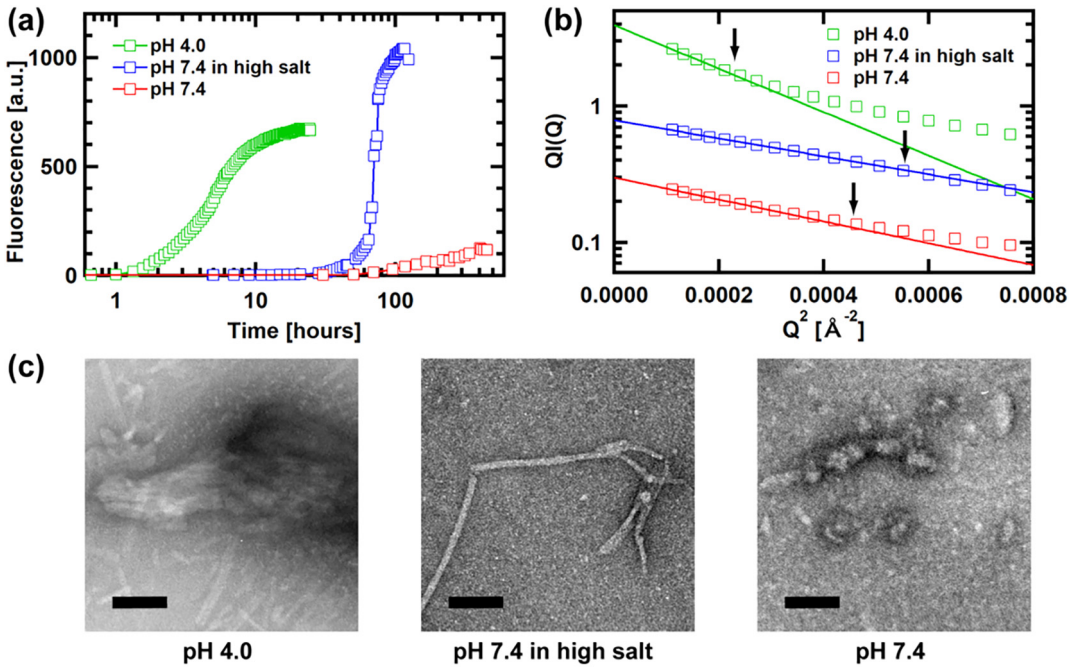

Fig. 1. (a) Kinetics of aggregation of αSyn under different solution conditions, monitored by ThT fluorescence. (b) The cross-sectional Guinier plots of the SAXS curves of αSyn fibrils (or aggregates) under different conditions. Arrows indicate the maximum Q values of the Guinier regions, Q_{max}, specified by $Q_{max}R_c$ = 1.3. Errors bars within symbols are not shown. (c) Examples of the EM images at the final states of the aggregation kinetics under different conditions. A scale bar of 100 nm is shown in each image.

at pH 4.0 shows the fast kinetics with a lag time of at most 1 h and reaching a plateau at about 20 h, whereas the kinetics of the solution at pH 7.4 in high salt shows a lag time of about 20 h and reaching a plateau at about 100 h. Furthermore, the solution at pH 7.4 without salt shows very slow kinetics with a lag time of about 50 h, and it takes at least 400 h to reach a plateau. The degrees of aggregation at the plateaus were evaluated by measuring the concentrations of the solutions in the initial state and the supernatants after centrifugation of the solutions in the plateau state. It was found that the degrees of aggregation were 98% and 96% for the solutions at pH 4.0 and at pH 7.4 in high salt, respectively. On the other hand, the degree of aggregation was 38% for the solution at pH 7.4 without salt. This indicates that, together with the low fluorescence intensity of ThT, which increases when the dye binds to the fibrils, the fibril formation is not completed under this condition. The fluorescence intensity at the plateau at pH 4.0, which is lower than at pH 7.4 in high salt, should be related to the different morphology of the aggregates formed.

The structures of fibrils or aggregates formed under these conditions were characterized using SAXS. The SAXS measurements were carried out on the αSyn solutions at pH 7.4 in high salt, at pH 7.4, and at pH 4.0, after reaching the plateau states through incubation at 37 °C with constant stirring. The SAXS curves, $I(Q)$, where Q (=$4\pi\sin\theta/\lambda$, 2θ is the scattering angle and λ is the wavelength of x-ray) is the momentum transfer, were analyzed using the cross-sectional Guinier plots (the Q^2 *versus* $\ln(QI(Q))$ plots, see Materials and Methods). Figure 1(b) shows the cross-sectional Guinier plots. A slope of a linear fit to this plot provides the cross-sectional radius of gyration (R_c) of a filamentous structure. The plot of αSyn at pH 7.4 in high salt shows clearly a linear region, which extends beyond the Guinier region, the maximum Q-value of which is specified by the relationship, QR_c = 1.3 [41], indicating a well-defined filamentous structure. The value of R_c was 55.2 ± 0.3 Å, which corresponds to the radius of 78 Å, assuming a solid cylinder. This size of the fibrils is consistent with the previous studies [32,34]. On the other hand, the plot of αSyn at pH 4.0 shows a rather limited linear region, from which R_c was estimated to be 85.7 ± 1.2 Å. This R_c value corresponds to a solid cylinder with a radius of 121 Å, which is somewhat smaller than twice the radius of the cylinder corresponding to the fibril structure at pH 7.4 in high salt. This implies that two fibril structures associate or crush at pH 4.0. The cross-sectional Guinier plot of αSyn at pH 7.4 without salt provided the R_c value of 60.8 ± 1.4 Å. However, the curve deviates from a linear region, while it is within the Guinier region. This is likely due to the low degree of aggregation (38%) under this condition.

Morphology of the aggregates formed under these conditions was examined with electron microscopy

(EM). Figure 1(c) shows examples of the EM images. At pH 7.4 in high salt, many long fibrils were observed. On the other hand, at pH 7.4 without salt, the fibrils appear to be shorter and irregular, suggesting that they are not completely fibrillar. Furthermore, the number of fibrils observed was significantly smaller than that at pH 7.4 in high salt, but small structures with rather globular shapes were frequently observed. At pH 4.0, many short fibrils were clumped together to form aggregates. These observations are consistent with the results of the SAXS measurements. Thus, the solution conditions at pH 7.4 in high salt, pH 4.0, and at pH 7.4 represent the conditions under which mature fibrils are formed, short fibrils are clumped to form large aggregates, and fibril formation is not completed, respectively.

Structural characterization of the monomeric states in various solution conditions

The fact that changes in the solution condition result in changes in the aggregation behavior implies that the behavior of αSyn monomers underlies the aggregation behavior. It is therefore important to characterize the behavior of αSyn in the monomeric state for elucidating the different aggregation behavior. We investigated the structural and dynamic properties of αSyn in the monomeric states under these solution conditions.

It is expected that αSyn is in the monomeric state when the solutions are not incubated at 37 °C with constant stirring. To verify this, we carried out the dynamic light scattering (DLS) measurements on the αSyn solution at pH 7.4 in high salt, pH 7.4 without salt, and pH 4.0. Note that the measurements were done on the samples under the similar conditions to those for the QENS measurements (similar protein concentrations in the buffers in D_2O) to make comparison of the diffusion coefficients possible (see below), and thus pH for the DLS samples was actually pD as for the QENS measurements. Figure 2(a) shows examples of the distribution of the decay time, obtained from the DLS measurements. The distributions show single peaks. Although the small peaks due to large aggregates are observed for the samples pH 7.4 and pH 4.0, the weights for the main peaks are more than 97%, indicating that the αSyn molecules in these solutions can be considered monomeric. Figure 2(b) shows examples of the Q dependence of the decay rate, which is inverse of the decay time. A slope of a linear fit to the plot provides the value of the translational diffusion coefficient (D_T). The values of D_T are summarized in Fig. 6(a) and Table S1 in the supplemental information. These values were used to simulate the apparent diffusion coefficient from the QENS spectra.

As αSyn in these solutions was verified to be monomeric, the SAXS measurements were carried out on these solutions. For each solution, a concentration series of the measurements were carried out

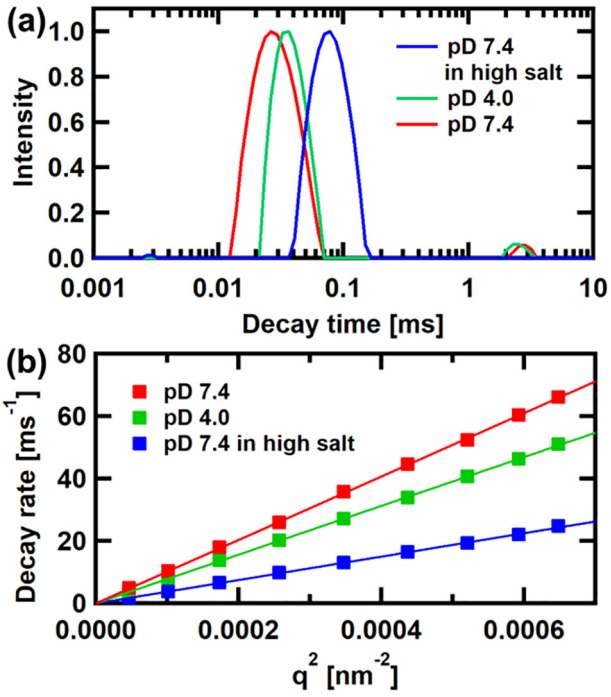

Fig. 2. (a) Examples of the decay time distributions, obtained from the DLS measurements. The distributions at the scattering angle (2θ) of 90° at 287 K are shown. (b) Examples of the plots of the decay rate against Q^2 ($Q = 4\pi n \sin\theta/\lambda_0$, where n is the refractive index and λ_0 is the wavelength of the laser). The plots of the solutions at 287 K are shown.

between αSyn concentrations of 1.8 and 5.5 mg/ml. Examples of the SAXS curves are shown in Fig. 3(a). The small-angle regions of these SAXS curves were analyzed using the Guinier plot (the Q^2 *versus* $\ln I(Q)$ plot, see Materials and Methods), examples of which are shown in Fig. 3(b). The values of the radius of gyration, R_g, and $I(0)/c$, which is proportional to the molecular weight, obtained from linear fits to these plots, are summarized in the upper and lower panels of Fig. 3(c), respectively. There are little concentration dependences of these parameters. As shown in the upper panel of Fig. 3(c), the R_g values of αSyn at pH 7.4 in high salt are about 42 Å. This value is consistent with the values of αSyn monomers in the previous studies [43–45]. The values at pH 4.0 are about 33 Å, which is also consistent with the previous studies [43,44]. R_g becomes even smaller at pH 7.4 without salt, to be about 27 Å, indicating that αSyn at pH 7.4 adopts more compact structures than in high salt. On the other hand, as shown in the lower panel of Fig. 3(c), the $I(0)/c$ values are all similar between the samples under the different conditions, verifying again that αSyn is monomeric in these solutions. The maximum dimension (D_{max}) was estimated from the length-distribution ($p(r)$) function obtained using GNOM [46] in the program suit ATSAS [47]. As shown in Fig. 3 (d), D_{max} in the $p(r)$ functions of αSyn at pH 4.0 is

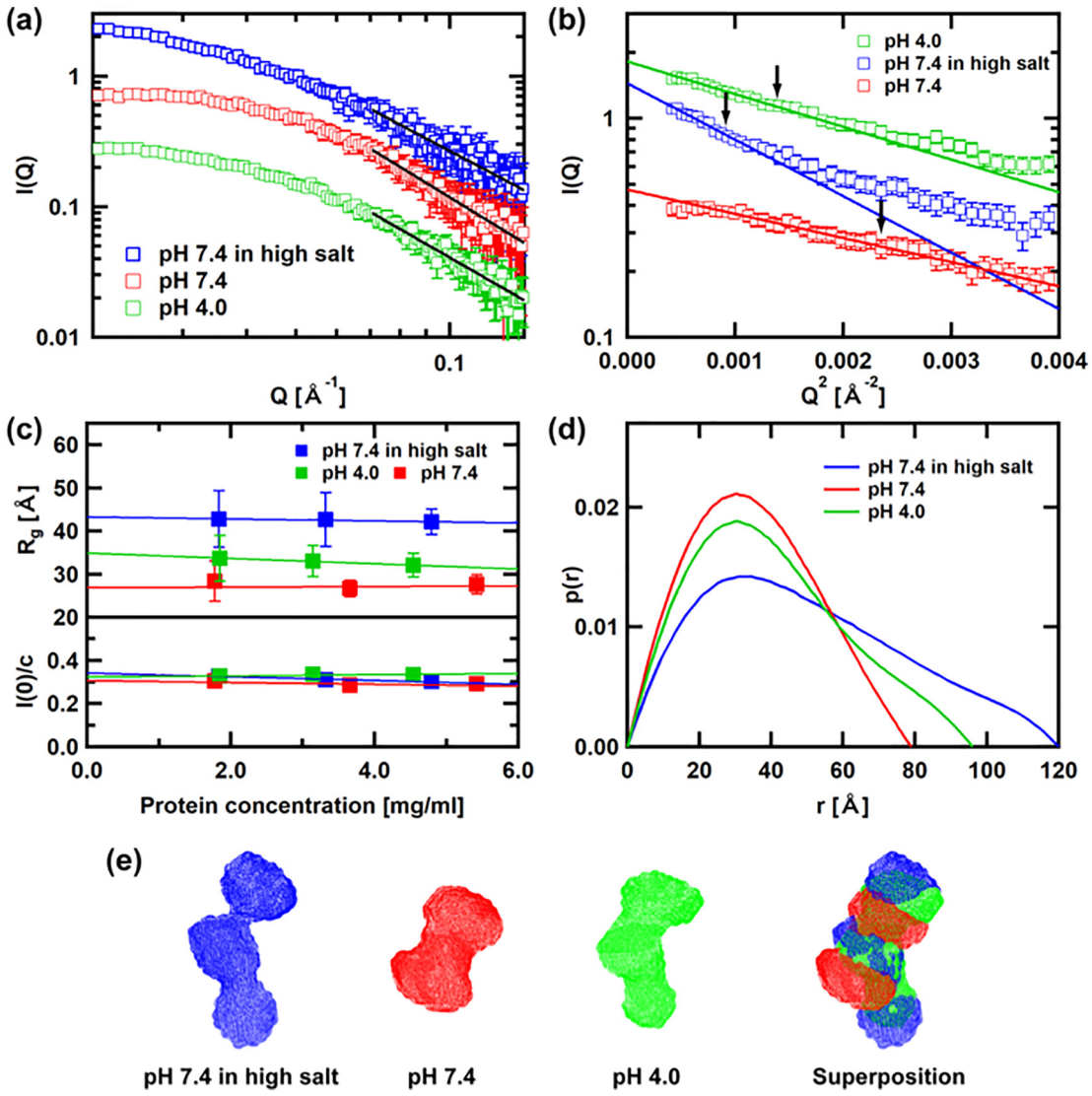

Fig. 3. (a) Examples of log–log plots of the SAXS curves of αSyn monomers under different conditions. Solid lines are the fits to the data in the high-angle region in the measured Q-region with the power–law relationship, $I(Q) \propto Q^{-Dm}$. (b) Examples of the Guinier plots of the data in the small-angle region of the SAXS curves. Arrows indicate the maximum Q values of the Guinier regions, Q_{max}, specified by $Q_{max}R_g = 1.3$. (c) The concentration dependences of R_g and $I(0)/c$, evaluated from the Guinier plots. (d) The $p(r)$ functions of αSyn monomers under different conditions. (e) The dummy-atom models for αSyn monomers under different conditions. The averaged models with volume correction over the 100 models generated are shown. The picture on the right is the superposition of the averaged models for the different conditions.

smaller than that at pH 7.4 in high salt, and D_{max} at pH 7.4 without salt is smaller than that at pH 4.0, again indicating that the molecules are more compact.

Such changes in the compactness may be reflected in the behavior of the high-angle region in the SAXS curves. Fits to the curves in these regions with the power-law relationship, $I(Q) \propto Q^{-Dm}$, shown in Fig. 3(a), provide the fractal dimensions, D_m, of 2.06 ± 0.18, 2.24 ± 0.13, and 2.39 ± 0.19 for the curves at pH 7.4 in high salt, at pH 4.0, and at pH 7.4 without salt, respectively. The D_m values of 2 and 3 correspond to the power laws of a Gaussian chain, which is often employed as a model of an unfolded protein, and the molten-globule state of proteins, respectively [48]. The conformations of αSyn are thus similar to those represented by the Gaussian chain. An increase in the compactness of the conformations appears to be accompanied by an increase in the D_m values. This implies that the conformations of αSyn, which can be approximated by the extended Gaussian chain at pH 7.4 in high salt, tend to change toward the more molten-globule-like conformations at pH 4.0 and at pH 7.4 without salt.

We employed a modeling approach for further analysis. We constructed dummy-atom models for

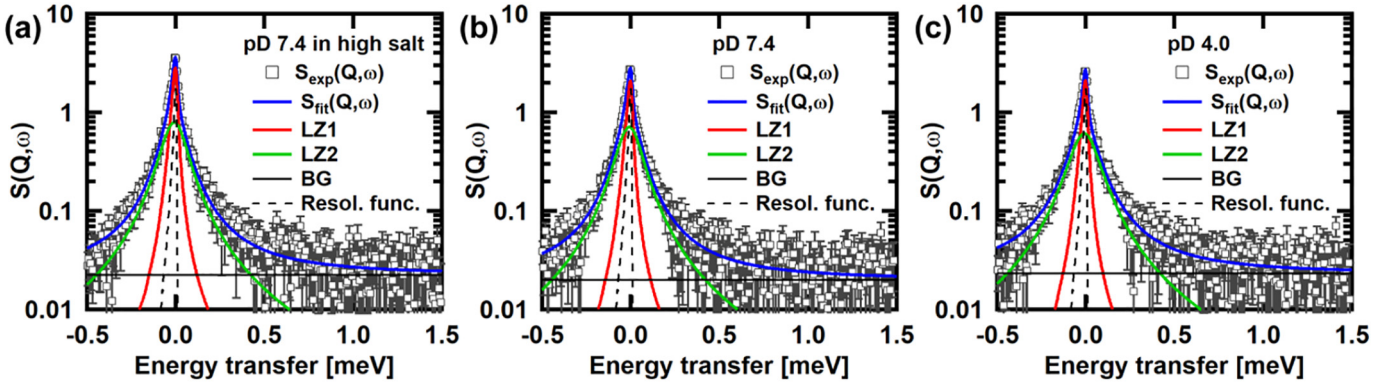

Fig. 4. Examples of the QENS spectra. The spectra at $Q = 1.05$ Å^{-1} of αSyn monomers (a) at pD 7.4 in high salt at 277 K, (b) at pD 7.4 at 280 K, and (c) at pD 4.0 at 280 K are shown. The fits to the experimental spectra using Eq. (1) and the resolution function are also shown.

these samples using DAMMIF [49] in ATSAS. One hundred dummy-atom models generated for each condition were averaged using DAMMAVER [50] in ATSAS. Fig. S2 in the supplemental information shows examples of the models generated. The averaged models over the hundred models generated are shown in Fig. 3(e). These models are consistent with the order of compactness indicated by R_g and D_{max} (pH 7.4 without salt ≪ pH 4.0 ≪ pH 7.4 in high salt). Superposition of these models, done by using SUPCOMB [51] in ATSAS, is also shown in Fig. 3(e). Assuming that the central regions in these models, which are superposed in Fig. 3(e), are the NAC region, the flexible N- and C-terminal regions are more expanded at pH 7.4 in high salt than those at pH 4.0 and at pH 7.4 without salt. The overall structure of αSyn thus changes corresponding to the changes in the solution condition.

As an alternative modeling approach to analyze the SAXS curves, we also employed the ensemble optimization method (EOM), in which an ensemble of conformations is selected to fit the SAXS curve out of a large pool of (randomly generated) conformations, and which has been shown to be useful to analyze flexible proteins [52]. We carried out the EOM analysis using the program EOM [53] in ATSAS. The results of the EOM analysis were essentially similar to those from the dummy-atom models, with the exception of including highly extended conformations in the ensemble for the condition at pH 7.4 in high salt. The details of the results and the discussion on the results are described in Text S1 in the supplemental information. Although some cautions are made, the conclusions are the same as those obtained from the dummy-atom models.

Dynamic characterization of the monomeric states in various solution conditions

The differences in the "averaged" structures of αSyn monomers reflect the differences in the distributions of the conformational ensembles between the solution conditions. This implies that the dynamic properties underlying the conformational ensembles are different between the solution conditions. We thus characterized the dynamic properties of the αSyn monomers in these solutions using QENS. The QENS measurements were carried out on the solutions in D_2O so that the signals from the hydrogen atoms in proteins can be detected with the minimum influence of the solvent signals. Figure 4 shows examples of the QENS spectra of αSyn at pD 7.4 in high salt, at pD 7.4, and at pD 4.0 at $Q = 1.05$ Å^{-1}. The spectra, $S(Q,\omega)$, where ω is the energy transfer of neutrons, can be fit with the equation [54]:

$$S(Q,\omega) = [A_0(Q)\delta(\omega) + \{1-A_0(Q)\}L_{local}(Q,\omega)] \otimes L_{global}(Q,\omega) \otimes R(Q,\omega) + B(Q), \quad (1)$$

where $A_0(Q)\delta(\omega)$ is the elastic component with $A_0(Q)$ being the elastic incoherent structure factor (EISF) and $\delta(\omega)$ being the Dirac delta-function. $L_{local}(Q,\omega)$ and $L_{global}(Q,\omega)$ are the Lorentzian functions describing the local atomic motions within the proteins ($L_{local}(Q,\omega) = (1/\pi) \times (\Gamma_{local}(Q)/(\Gamma_{local}(Q)^2 + \omega^2))$) and the global diffusive motions of the proteins ($L_{global}(Q,\omega) = (1/\pi) \times (\Gamma_{global}(Q)/(\Gamma_{global}(Q)^2 + \omega^2))$), respectively, where $\Gamma_{local}(Q)$ and $\Gamma_{global}(Q)$ denote the half-width at half-maximum (HWHM) of the corresponding Lorentzian functions. $R(Q,\omega)$ is the instrumental resolution function, which is obtained from the spectra of vanadium, $B(Q)$ is the background, and $\otimes$ denotes the convolution operation. The results of the fits are also shown in Fig. 4. Using this phenomenological equation based on the assumption that the global motions and local motions are uncorrelated, the contributions of the global motions and the local motions of αSyn can be separated.

The global motions of αSyn can be characterized by $L_{global}(Q,\omega)$. In particular, analysis of $\Gamma_{global}(Q)$ provides information on the diffusive motions of αSyn. Figure 5 shows the Q^2 dependence of $\Gamma_{global}(Q)$. $\Gamma_{global}(Q)$ increases linearly with increasing Q^2, indicating that the motions observed can be regarded as free diffusion. The apparent diffusion coefficient, D_{app}, can then be evaluated according to the relationship, $\Gamma_{global}(Q) = D_{app}Q^2$. The values obtained are summarized in Fig. 6. Although the differences in the D_{app} values (filled squares) between the different solution conditions are small, these values are significantly larger than the D_T values (crosses) obtained from the DLS measurements. It has been shown that D_{app} contains the contributions from not only translational diffusion but also rotational diffusion of the entire particle [40,55–58]. The spectra arising from the translational and rotational diffusion were thus simulated, based on the D_T values obtained from the DLS measurements and the rotational diffusion coefficients (D_R) calculated from the dummy-atom models obtained from the SAXS measurements (see Text S2 in the supplemental information for details of the calculation). The simulated spectra were well approximated by single Lorentzian functions, and linear fits to the Q^2 dependence of the HWHM provide the simulated values of D_{app} (see Fig. S4 in the supplemental information). The open circles in Fig. 6(a) are the simulated D_{app} values. There is still a significant discrepancy between the experimental and simulated D_{app} values. The contribution of the rotational diffusion to the simulated values may be somewhat smaller than expected: The ratios, D_{app}/D_T, fall in a range between 1.1 and 1.28, while these ratios are about 1.27 for globular proteins [40]. The D_R values employed in the simulations were calculated from the dummy-atom models using HYDRO++ [59], based on the rigid-body assumption, to be about $1–3 \times 10^6$ s^{-1} as shown in Table S1 in the supplemental information. On the other hand, for example, D_R of hen egg white lysozyme, one of the

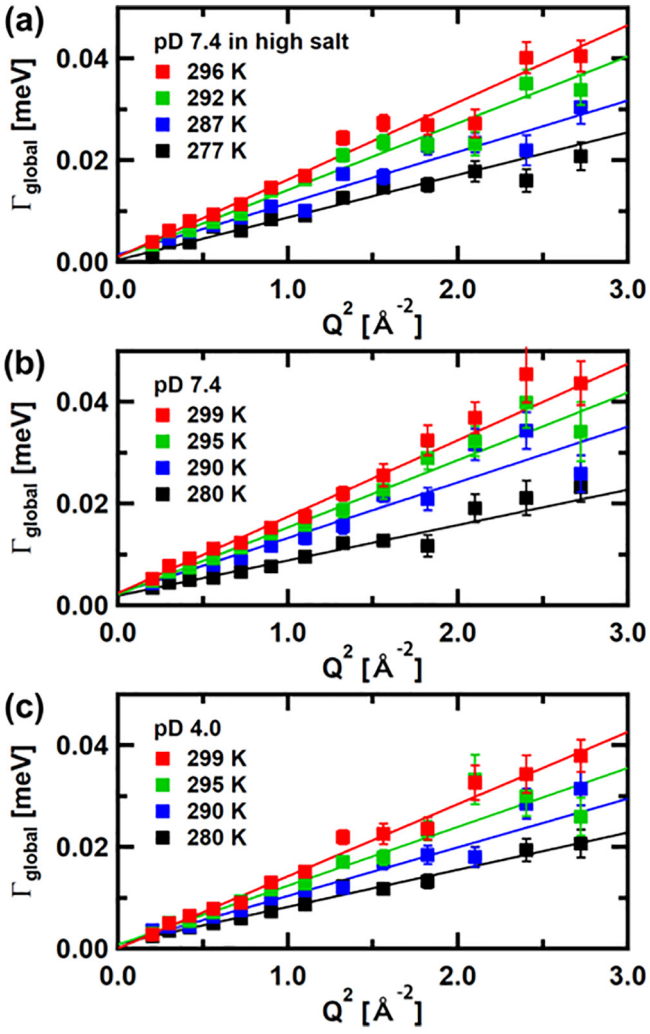

Fig. 5. Q^2 dependence of Γ_{global} of αSyn monomers (a) at pD 7.4 in high salt, (b) at pD 7.4, and (c) at pD 4.0. The results of the linear fits are also shown. Errors bars within symbols are not shown.

typical globular proteins with a similar molecular weight to αSyn, is calculated from the crystal structure (PDB code: 193L) to be 1.56×10^7 s^{-1}, using the program HYDROPRO [60]. Such significant differences in the D_R values could account for the relatively small contribution of the rotational diffusion on D_{app}.

The discrepancy between the experimental and simulated D_{app} values indicates that the significant internal motions such as segmental motions contribute to D_{app} as shown in the previous studies [29,61,62]. Figure 6(b) shows the differences between the dashed lines, which are the linear fits to the experimental D_{app} values above 285 K, and the dash-dotted lines, which are the linear fits to the simulated D_{app} values, in Fig. 6(a). This demonstrates the degree of contribution of the internal segmental motions to D_{app}. It is shown that this degree at pD 7.4 in high salt is about twice as large as that at pD 7.4 without salt and at pD 4.0, whereas they are similar between at pD 7.4 without salt and at pD 4.0. The degrees of the contribution of the internal segmental motions of αSyn are thus significantly larger at pD 7.4 in high salt than at pD7.4 without salt and at pD 4.0. Note that the conclusions were the same when the parameters obtained from the EOM analysis were employed (see Text S3 in the supplemental information.)

The previous study on unfolded proteins by QENS, however, showed consistency between the experimental and theoretical spectra and detected no contribution of additional motions [58]. This study employed the D_T and D_R values obtained from the neutron spin-echo (NSE) spectroscopy measurements [63], in which the analysis was based on the Zimm model, which regards polypeptides as a chain consisting of beads with uniform bond lengths, including internal friction. The values employed were thus those of each bead in a chain, which characterize the internal motions within the chain. The results of the study therefore indicate that the internal motions in the unfolded proteins contribute to the QENS spectra. This study, which detects the internal motions as the differences between the experimental values and the simulated values for a rigid body, provides a

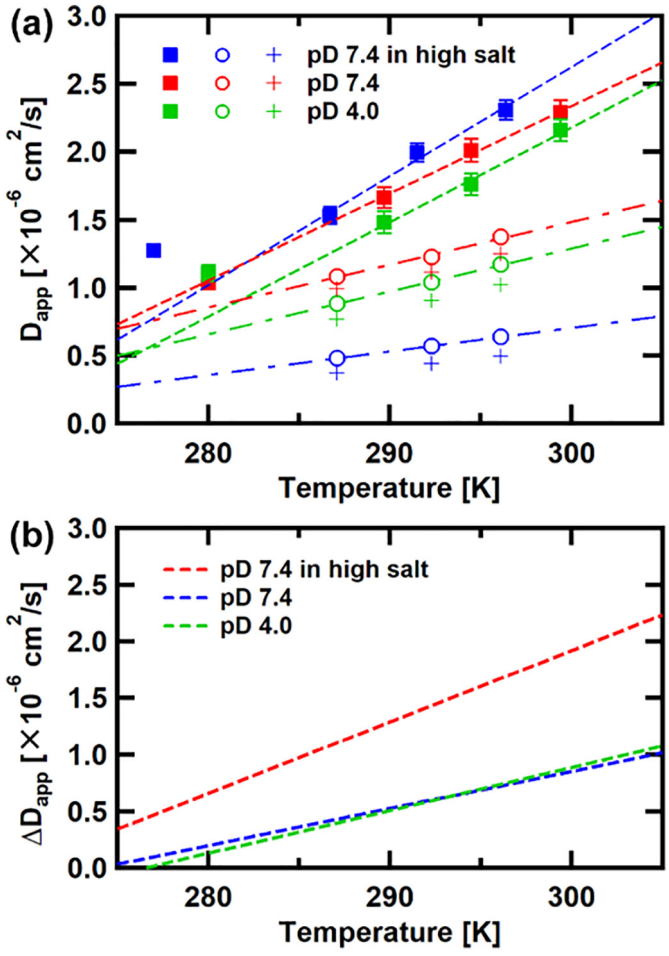

Fig. 6. (a) Summary of D_{app} obtained from the QENS spectra, D_{app} obtained from the simulation based on the DLS and SAXS measurements, and D_T obtained from the DLS measurements. Errors bars within symbols are not shown. Filled squares, open circles, and crosses denote the D_{app} values obtained from the QENS measurements, the D_{app} values from the simulation, and the D_T values from the DLS measurements, respectively. Dashed lines are the fits to D_{app} from QENS above 285 K, and dashed-dotted lines are the fits to the simulated D_{app}. (b) The difference curves between the dashed lines and the dashed-dotted lines shown in panel a.

complementary method to those combined with the NSE spectroscopy.

The local motions within the αSyn molecules such as fluctuations of the side chains can be characterized by $L_{local}(Q,\omega)$. In particular, analysis of $\Gamma_{local}(Q)$ provides information on the frequency of the local motions. Figure 7(a–c) shows the Q^2 dependence of $\Gamma_{local}(Q)$. The observed asymptotic behavior of $\Gamma_{local}(Q)$ can be described by an equation based on a jump-diffusion model, $\Gamma_{local}(Q) = D_{jump}Q^2/(1 + D_{jump}Q^2\tau)$, where D_{jump} is the jump-diffusion coefficient and τ is the residence time [54]. The results of the fits are also shown in Fig. 7(a–c). As a measure of the frequency of the local jumping motions, the residence times were compared between the different solution conditions. Figure 7(d) shows the Arrhenius plots of the residence time. The residence times of αSyn at pD 7.4 without salt are substantially larger than those at pD 7.4 in high salt and at pD 4.0. This suggests that the local motions under this condition are slower than those at pD 7.4 in high salt and at pD 4.0. The slopes of the Arrhenius plot provide the activation energy for the jumping motions according to the Arrhenius law, $\tau = \tau_0 \exp(-E_a/k_B T)$, where E_a is the activation energy, k_B is the Boltzmann constant, and T is the temperature. The evaluated activation energy is 7.5 ± 0.9, 6.8 ± 1.3, and 5.5 ± 0.9 kcal/mol for αSyn at pD 7.4 without salt, at pD 7.4 in high salt, and at pD 4.0, respectively. The activation energy of the local motions at pD 4.0 may be smaller than that under the conditions at pD 7.4.

The amplitude of the local motions can be evaluated by analyzing the EISF curve ($A_0(Q)$ in Eq. (1)), which is calculated as the ratio of the intensity of the elastic peak to the sum of the intensity of the elastic peak and that of quasielastic scattering. Figure 8 is a summary of the EISF curves. These EISF curves were fit with the equation based on the diffusion-inside-a-sphere model [64], in which each atom is assumed to undergo diffusive motion in a sphere of a certain radius, described as,

$$\mathrm{EISF}(Q) = p_0 + (1-p_0) \times (3j_1(Qa)/Qa)^2, \quad (2)$$

where p_0 denotes the "immobile" fraction of atoms, motions of which are outside the current instrumental energy window, $j_1(Qa)$ is the first order spherical Bessel function of the first kind, and a denotes the radius of the sphere, within which atoms undergo

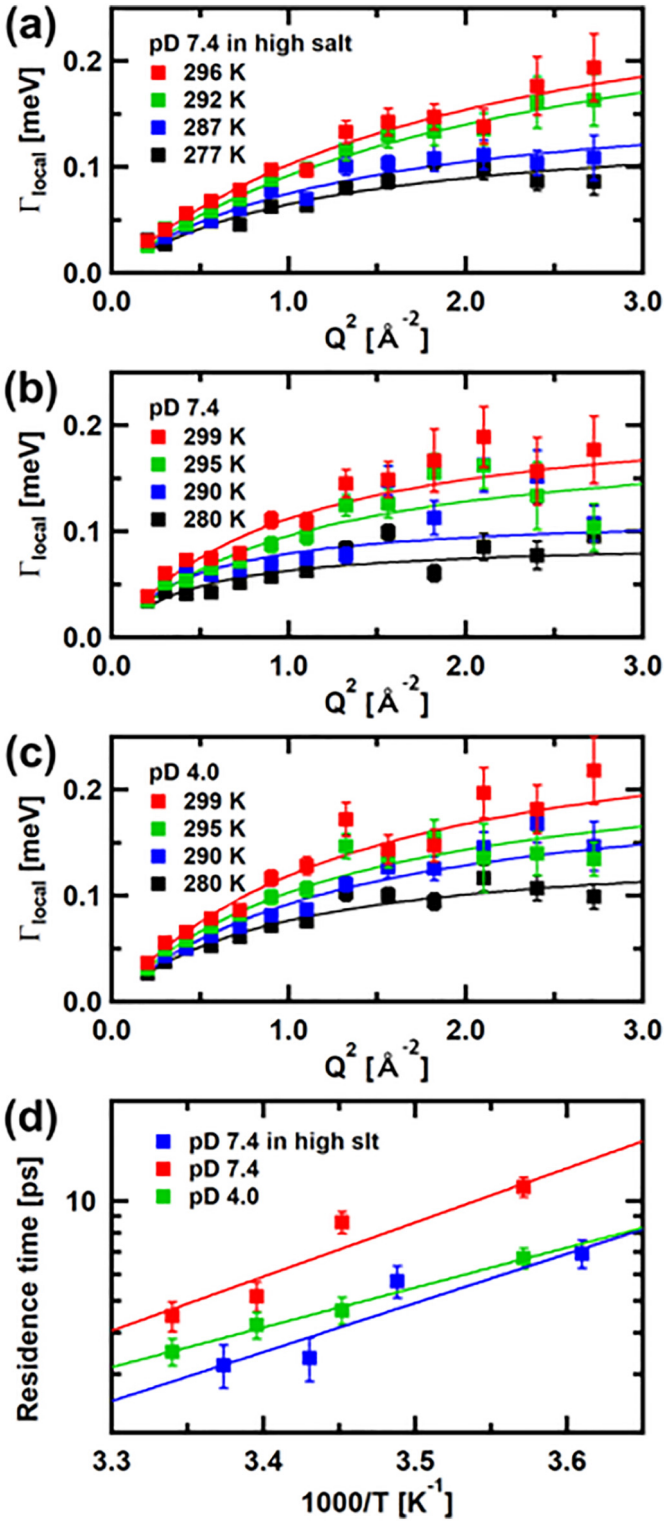

Fig. 7. Q^2 dependence of $\Gamma_{local}(Q)$ of αSyn monomers (a) at pD 7.4 in high salt, (b) at pD 7.4, and (c) at pD 4.0. Solid lines are the fits with the equation based on a jump-diffusion model. Error bars within symbols are not shown. (d) The Arrhenius plot of the residence time of the jump diffusion model, estimated from the fits shown in panels a, b, and c.

diffusive motions. The results of the fits are also shown in Fig. 8. Figure 9 summarizes the results of the fits. As shown in Fig. 9(a), the fractions of immobile atoms are similar between the different conditions. On the other hand, as shown in Fig. 9(b), the radius of the sphere is different between the conditions. In particular, the *a* values at pD 7.4 without salt are consistently lower than those at pD 7.4 in high salt and at pD 4.0, indicating that the amplitude of the local motions is enhanced at pD 7.4 in high salt and at pD 4.0.

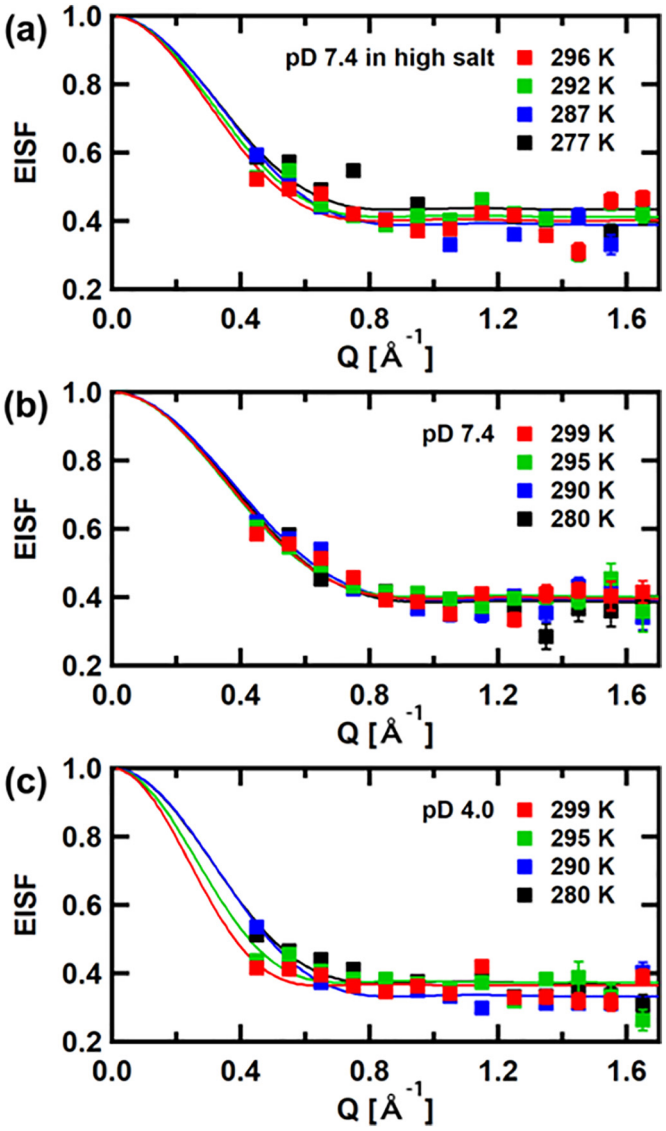

Fig. 8. The EISF curves of αSyn monomers (a) at pD 7.4 in high salt, (b) at pD 7.4, and (c) at pD 4.0. Solid lines denote the results of the fit with Eq. (2). Errors bars within symbols are not shown.

Moreover, whereas the *a* values are similar between pD 7.4 in high salt and at pD 4.0 below around 290 K, the values at pD 4.0 becomes larger than those at pD 7.4 in high salt above around 295 K. Thus, at the temperatures where the incubation for aggregation is carried out, the local motions are more enhanced under the conditions where large aggregates are formed by clumping of the short fibrils, compared to the conditions where mature amyloid fibrils are formed.

Discussion

In this study, the structural and dynamic properties of αSyn monomers were characterized. αSyn under the conditions showing the different propensities to fibril formation was shown to have distinct structural and dynamic properties. The SAXS measurements showed that at pH 7.4 in high salt, where αSyn forms mature fibrils, αSyn adopted disordered and expanded structures. At low pH where the short fibrils of αSyn tend to clump together to form large aggregates, these expanded structures became more compact such that the disordered N- and C-terminal regions came close to the central NAC region. The structures became even more compact at pH 7.4 without salt, where fibril formation is not completed. On the other hand, the QENS measurements showed that at pH 7.4, the segmental motions as well as the local motions such as the side-chain motions were enhanced in the presence of 150 mM NaCl. The local motions were enhanced in both frequency and amplitude. At pH 4.0, the segmental motions of αSyn were similar to those at pH 7.4 without salt, while the local motions were enhanced in both frequency and amplitude. In particular, the amplitude of the local motions was larger than that at pH 7.4 in high salt at the temperatures above 295 K.

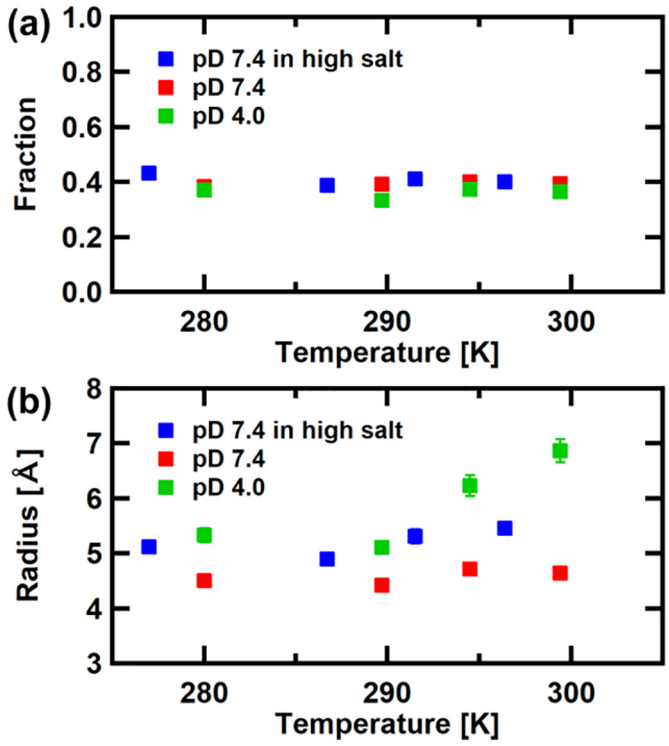

Fig. 9. Summary of the parameters of the models describing the EISF curves. Errors bars within symbols are not shown.

Enhancement of the intramolecular motions of αSyn is thus obviously related to adoption of the expanded structures. This enhancement would facilitate a wider distribution of the conformational ensemble, and the wider distribution is possible when the molecules are more expanded.

The structures of αSyn at neutral and low pH in the presence of high salt have been characterized using NMR and molecular dynamics simulation [23,27,65]. These studies provide a consistent picture as follows. At neutral pH, the C-terminal region in αSyn adopts extended conformations while the N-terminal and NAC regions have transient contacts between them, and the conformational ensemble has a wide distribution. On the other hand, at low pH, the contacts between the C-terminal and NAC regions are observed in addition to those between the N-terminal and NAC regions, and the C-terminal region itself is more compact than at neutral pH. The distribution of the conformational ensemble also becomes more homogeneous than that at neutral pH. Structural characterization using FRET [66,67] has shown consistently that lowering pH results in compaction of the molecule. Characterization of the structures of αSyn in the presence and absence of 150 mM NaCl at pH 6.0 using NMR has shown that the structures are more compact in the absence than in the presence of high salt [68]. These results are consistent with the results from the SAXS measurements in this study.

The structural characterization using NMR and FRET as above suggests long-range interactions, such as those between the N-terminal and NAC regions and between the C-terminal and NAC regions. Segmental motions within and between these regions have been indeed detected using the FRET techniques [19–21]. Such motions contribute to the global motions obtained from the QENS measurements in this study. The decrease in the contribution of the segmental motions to the global motions in the QENS spectra at low pH is consistent with the observation of the decrease in the intramolecular diffusion coefficients obtained by the FRET techniques [20,21]. Since lowering pH increases the contacts between the C-terminal and other regions while those between the N-terminal and NAC regions remain similar [27,65], this decrease is likely to arise from the decrease in the motions of the C-terminal region.

The decreased segmental motions occur concomitantly with the compaction of the molecule. These changes, observed not only at pH 4.0 but also at pH 7.4 without salt, are likely to protect the NAC region from interacting with other molecules. Nevertheless, at pH 4.0, the most of the molecules form large aggregates, whereas at pH 7.4 without salt, about 60% of the molecules remain monomeric and/or oligomeric states such that the molecules remain in the supernatant after ultracentrifugation. This difference should arise from another observed difference, namely the difference in the local motions in αSyn between pH 4.0 and pH 7.4 without salt. Both frequency and amplitude of the local motions

are enhanced at pH 4.0 to similar degrees to those at pH 7.4 in high salt. In particular, the amplitude of the local motions at pH 4.0 is larger than that at pH 7.4 in high salt above 295 K. The local motions thus need to be enhanced for aggregation to proceed. If, however, the NAC regions are protected as at pH 4.0, fibril formation, which requires the interactions between the NAC regions in different molecules, presumably competes with non-specific interactions arising from the overly enhanced local motions such as those observed at pH 4.0 above 295 K, and result in clumping of short fibrils to form large aggregates. The results obtained in this study thus imply that amyloid fibril formation of αSyn requires not only the enhanced local motions, but also the segmental motions that properly expose the NAC region so that interactions between the molecules are possible.

The importance of the enhanced intramolecular motions suggests that fibril formation can be inhibited by controlling the dynamics of αSyn. The NAC region has been the main target region for inhibitors because the binding of inhibitors to this region directly prevents the interactions leading to fibril formation. However, fixing the segmental motions of the C- and/or N-terminal regions in the positions to shield the NAC region should be able to inhibit fibril formation as well. These regions can therefore be candidates for the target for the inhibitors [23]. Furthermore, the inhibition of the local dynamics should also be effective in inhibiting fibril formation. Since the local motions detected by QENS are averaged motions over the entire molecule, the possible key region(s), the local motions in which are particularly important for fibril formation, cannot be specified. More detailed analysis of the spectra with the aid of, for example, molecular dynamics simulation could provide information on such regions. Including these regions as the potential targets would expand the possibility of developing new inhibitors. The possibility of inhibiting fibril formation by controlling the dynamics should thus provide a possibility of new strategy of drug development based on the dynamics of the target molecules.

Materials and Methods

Sample preparation

Human wild-type αSyn was expressed in *Escherichia coli* BLR(DE3), and purified as described [69]. The purified protein was suspended either in solution containing 20 mM Hepes (pH 7.4), containing 20 mM Hepes (pH 7.4) and 150 mM NaCl, or containing 20 mM sodium acetate (pH 4.0), by dialysis. These sample solutions were prepared in either H_2O or D_2O. For the SAXS, DLS, and QENS experiments, the sample solutions were ultracentrifuged at 100,000*g* for 20 min to remove any aggregates just before starting the measurements.

Aggregation kinetics measurements

The kinetics of the aggregation of αSyn was monitored by the fluorescence measurements of ThT. The αSyn solutions at pH 7.4 without salt, at pH 7.4 in high salt, and at pH 4.0 were prepared in H_2O at concentrations of about 2 mg/ml. The concentration of αSyn was determined spectrophotometrically using an extinction coefficient of $\varepsilon_{280\ \mathrm{nm}}^{0.1\%} = 0.354$ [70]. ThT was added to each solution at the final concentration of 20 μM. These solutions were put into the quartz cuvettes for the fluorescence measurements and incubated at 37 °C under constant stirring with micro stirrer bars in a fluorescence spectrophotometer F-7000 (Hitachi Hi-Technologies Corp., Tokyo, Japan). The fluorescence measurements of ThT were carried out continuously during the incubation.

SAXS measurements

The sample solutions at pH 7.4 without salt, at pH 7.4 in high salt, and at pH 4.0 were prepared in H_2O with the protein concentrations between 1.8 and 5.5 mg/ml. The fibril (or aggregate) solutions of αSyn under these conditions were prepared at αSyn concentrations of 3 mg/ml by incubating the solutions at 37 °C with constant stirring. The measurements of the scattering patterns were carried out using the beamline BL8S3 in Aichi Synchrotron Radiation Center, Aichi, Japan, with the wavelength (λ) of incident x-ray of 1.50 Å at 293 K. The sample-to-detector distance was 2.176 m. The scattering patterns were recorded using a pixel detector (PILATUS 100 K, Dectris) and were circularly averaged to obtain one-dimensional scattering curves. The intensity of these curves was corrected by the incident beam flux measured with an ion chamber placed upstream of the samples. The net scattering curves of the proteins were obtained by subtracting the scattering curves of the buffer from those of the samples.

Analysis of the scattering curves

The net scattering curves were analyzed using the Guinier plots [71]. For globular particles, the scattering curves in the small-angle region can be approximated by the equation,

$$I(Q) = I(0)\ \exp\left(-{R_g}^2 Q^2/3\right), \qquad (3)$$

where $I(0)$ is the scattering intensity at $Q = 0$, and R_g denotes the radius of gyration of the particle of interest. The plot of $\ln I(Q)$ against Q^2 (the Guinier plot) is thus fit by a straight line. The slope of the linear fit provides the value of R_g, and the molecular

weight of a particle of interest can be estimated from the $I(0)$ value. For filamentous particles such as amyloid fibrils, the scattering curve decreases with a factor $1/Q$, and the scattering curves in the small-angle region can be approximated as,

$$QI(Q) = I_c(0)\ \exp\left(-{R_c}^2 Q^2/2\right), \qquad (4)$$

where $I_c(0)$ is proportional to the mass per unit length of the filaments, and R_c is the cross-sectional radius of gyration. The linear fit to the plot of $\ln(QI(Q))$ against Q^2 (the cross-sectional Guinier plot) thus provides the values of R_c and the mass per unit length.

Further analysis for estimating the length distribution functions and generating the dummy-atom models were carried out using the program suite for small-angle scattering data analysis from biological macromolecules, ATSAS [46].

Electron microscopy

The final states of the sample solutions were examined with EM. A drop of each sample solution was applied to a glow-discharged carbon-coated copper grid, blotted, stained with 2% uranyl acetate, and visualized under a Hitachi H-7600 transmission electron microscope operated at 100 keV. Images were recorded on Fuji FG film at 20,600× magnification, and digitized with a EPSON GT-X970 flatbed scanner in 10.6-μm steps.

DLS measurements

The solutions of αSyn at pD 7.4 without salt, pD 7.4 in high salt, and pD 4.0 were prepared in D_2O with protein concentrations of about 10 mg/ml. These sample solutions were similar to those for the QENS measurements. The DLS measurements on these solutions were carried out using a system consisting of a 22-mW He–Ne laser (wavelength, λ_0 = 632.8 nm), an avalanche photodiode mounted on a static/dynamic compact goniometer, ALV/LSE-5004 electronics and an ALV-7004 correlator (ALV, Langen, Germany). The measurements were made at scattering angles from 30° to 120° in 15° steps, at temperatures at 15 °C, 20 °C, and 25 °C. The CONTIN analysis [72] was employed for the data analysis.

QENS measurements

The sample solutions similar to those for the DLS measurements as above were prepared. About 2 ml of the sample solutions was put into a double-cylindrical aluminum cell with a sample thickness of 1.0 mm, and sealed with indium wire. The QENS measurements were carried out using the near-backscattering spectrometer, BL02 (*DNA*), [73] at the Materials and Life Science Experimental Facility (MLF) of the Japan Accelerator Research Complex (J-PARC), Tokai, Ibaraki, Japan. The measurements were done at the energy resolution of 12 μeV, at which atomic motions faster than 55 ps are accessible, and at four temperatures between 280 K and 300 K. The QENS spectra of the solution samples and the D_2O buffers were measured.

The measured QENS spectra, $S(Q, \omega)$, were corrected for the empty cell contribution and the detector efficiency, and normalized to the vanadium standard, which was also used for defining the instrumental energy resolution. Subtraction of the spectra of the D_2O buffer from those of the D_2O-solution samples was done using the scaling factors calculated from the scattering cross-section of the samples [29]. Examples of the QENS spectra of the sample solutions, the buffer, and the difference between the spectra of the sample solutions and the buffer are shown in Fig. S6(a–c) in the supplemental information. The spectra thus obtained were verified by the static structure factor, $S(Q)$, calculated by integrating the $S(Q, \omega)$ along the ω-direction, examples of which are shown in Fig. S6(d–f). The QENS spectra of the D_2O-solution samples and the D_2O buffer show increase in intensity at $Q \gg \sim 1.4$ Å^{-1}, which arises from the coherent scattering of D_2O [74,75]. On the other hand, the spectra of the proteins do not contain such a contribution [75,76]. Proper subtraction of the D_2O-buffer spectra thus provides $S(Q)$ with rather flat intensity at $Q \gg \sim 1.4$ Å^{-1}. As shown in Fig. S6(d–f), whereas the increase in intensity at $Q \geq 1.4$ Å^{-1} is observed in the curves of the solution sample and the buffer, such an increase disappears in the difference curves. This indicates that the solvent contribution is negligible in the difference spectra, and thus, these difference spectra can be regarded as the spectra arising from the proteins. It should be noted that the increase in intensity observed in the region $Q \leq 0.4$ Å^{-1} arises from the coherent scattering of the protein [74,76]. Analysis was thus done on the spectra in the region $Q \gg 0.4$ Å^{-1}.

Acknowledgments

We thank Dr. S. Takata for his help in the DLS measurements. This work was supported in part by JSPS KAKENHI Grant Numbers 26293210 and 16 K13730 (to S.F.). The QENS experiments at J-PARC MLF were performed under the user programs (Proposal Nos. 2014B0156, 2016I0002, and 2017I0002). The SAXS experiments were carried out at BL8S3 of Aichi Synchrotron Radiation Center, Aichi Science & Technology Foundation, Aichi, Japan (Experimental Nos. 201606088 and 201706065).

Appendix A. Supplementary data

Supplementary data to this article can be found online at https://doi.org/10.1016/j.jmb.2019.05.047.

Received 28 January 2019;
Received in revised form 11 May 2019;
Available online 8 June 2019

Keywords:
small-angle x-ray scattering;
quasielastic neutron scattering;
dynamic light scattering;
Parkinson's disease;
intrinsically disordered protein

Abbreviations used:
PD, Parkinson's disease; αSyn, α-synuclein; NAC, non-amyloid-β component; FRET, Förster resonance energy transfer; NMR, nuclear magnetic resonance; QENS, quasielastic neutron scattering; SAXS, small-angle x-ray scattering; Hepes, 4-(2-hydroxyethyl)-1-piperazineethanesulfonic acid; ThT, thioflavin T; DLS, dynamic light scattering; EISF, elastic incoherent structure factor.

References

[1] M. Goedert, Alpha-synuclein and neurogenerative diseases, Nat. Rev. Neurosci. 2 (2001) 492–501.
[2] M.G. Spillantini, M.L. Schmidt, V.M.-Y. Lee, J.Q. Trojanowski, R. Jakes, M. Goedert, α-Synuclein in Lewy bodies, Nature 388 (1997) 839–840.
[3] M.H. Polymeropoulos, C. Lavedan, E. Leroy, S.E. Ide, A. Dehejia, A. Dutra, B. Pike, H. Root, J. Rubenstein, R. Boyer, E.S. Stenroos, S. Chandrasekharappa, A. Athanassiadou, T. Papapetropoulos, W.G. Johnson, A.M. Lazzaroni, R.C. Duvoison, G. Di Iorio, L.I. Golbe, R.L. Nussbaum, Mutation in the α-synuclein gene identified in families with Parkinson's disease, Science 276 (1997) 2045–2047.
[4] R. Krüger, W. Kuhn, T. Müller, D. Woitalla, M. Graeber, S. Kösel, H. Przuntek, J.T. Epplen, L. Schöls, O. Riess, Ala30Pro mutation in the gene encoding α-synuclein in Parkinson's disease, Nat. Genet. 18 (1998) 106–108.
[5] J.J. Zarranz, J. Alegre, J.C. Gómez-Esteban, E. Lezcano, R. Ros, I. Ampuero, L. Vidal, J. Hoenicka, O. Rodriguez, B. Atarés, V. Llorens, E.G. Tortosa, T. del Ser, D.G. Muñoz, J.G. de Yebenes, The new mutation, E46K, of α-synuclein causes Parkinson and Lewy body dementia, Ann. Neurol. 55 (2004) 164–173.
[6] S. Appel-Cresswell, C. Vilarino-Guell, M. Encarnacion, H. Sherman, I. Yu, B. Shah, D. Weir, C. Thompson, C. Szu-Tu, J. Trinh, J.O. Aasly, A. Rajput, A.H. Rajput, A.J. Stossel, M.J. Farrer, Alpha-synuclein p.H50Q, a novel pathogenic mutation for Parkinson's disease, Mov. Disord. 28 (2013) 811–813.
[7] S. Lesage, M. Anheim, F. Letournel, L. Bousset, A. Honoré, N. Rozas, L. Pieri, K. Madiona, A. Dürr, R. Melki, C. et Verny, A. Brice, G51D α-synuclein mutation causes a novel parkinsonian–pyramidal syndrome, Ann. Neurol. 73 (2013) 459–471.
[8] P. Pasanen, L. Myllykangas, M. Siitonen, A. Raunio, S. Kaakkola, J. Lyytinen, P.J. Tienari, M. Pöyhönen, A. Paetau, Novel α-synuclein mutation A53E associated with atypical multiple system atrophy and Parkinson's disease-type pathology, Neurobiol. Aging 35 (2180) (2014) e1–e5.
[9] A.B. Singleton, M. Farrer, J. Johnson, A. Singleton, S. Hague, J. Kachergus, M. Hulihan, T. Peuralinna, A. Dutra, R. Nussbaum, S. Lincoln, A. Crawley, M. Hanson, D. Maraganore, C. Adler, M.R. Cookson, M. Muenter, M. Baptista, D. Miller, J. Blancato, J. Hardy, K. Gwinn-Hardy, α-Synuclein locus triplication causes Parkinson's disease, Science 302 (2003) 841.
[10] M.-C. Chartier-Harlin, J. Kachergus, C. Roumier, V. Mouroux, X. Douay, S. Lincoln, C. Levecque, L. Larvor, J. Andrieux, M. Hulihan, N. Waucquier, L. Defebvre, P. Amouyel, M. Farrer, A. Destee, α-Synuclein locus duplication as a cause of familial Parkinson's disease, Lancet 364 (2004) 1167–1169.
[11] P. Ibanez, A.-M. Bonnet, B. Debarges, E. Lohmann, F. Tison, P. Pollak, Y. Agid, A. Durr, A. Brice, Causal relation between α-synuclein gene duplication and familial Parkinson's disease, Lancet 364 (2004) 1169–1171.
[12] P.H. Weinreb, W. Zhen, A.W. Poon, K.A. Conway, P.T. Lansbury Jr., NACP, a protein implicated in Alzheimer's disease and learning, is natively unfolded, Biochemistry 35 (1996) 13709–13715.
[13] L. Maroteaux, J.T. Campanelli, R.H. Scheller, Synuclein: a neuron-sepcific protein localized to the nucleus and presynaptic nerve terminal, J. Neurosci. 8 (1988) 2804–2815.
[14] J.T. Bendor, T.P. Logan, R.H. Edwards, The function of α-synuclein, Neuron 79 (2013) 1044–1066.
[15] V.N. Uversky, Looking at the recent advances in understanding α-synuclein and its aggregation through the proteoform prism, F1000Research 6 (2017) 525.
[16] L. Breydo, J.W. Wu, V.N. Uversky, α-Synuclein misfolding and Parkinson's disease, Biochim. Biophys. Acta 1822 (2012) 261–285.
[17] H. Mochizuki, C.-J. Choong, E. Masliah, A refined concept: α-synuclein dysregulation disease, Neurochem. Int. 119 (2018) 84–96.
[18] V.N. Uversky, Unusual biophysics of intrinsically disordered proteins, Biochim. Biophys. Acta 1834 (2013) 932–951.
[19] A. Grupi, E. Haas, Segmental conformational disorder and dynamics in the intrinsically disordered protein α-synuclein and its chain length dependence, J. Mol. Biol. 405 (2011) 1267–1283.
[20] B. Ahmad, Y. Chen, L.J. Lapidus, Aggregation of α-synuclein is kinetically controlled by intramolecular diffusion, Proc. Natl. Acad. Sci. U. S. A. 109 (2012) 2336–2341.
[21] V.C. Ducas, E. Rhodes, Investigation of intramolecular dynamics and conformations of α-, β-, and γ-synuclein, PLoS One 9 (2014), e85983.
[22] R. Bussel Jr., D. Eliezer, Residual structure and dynamics in Parkinson's disease-associated mutants of α-synuclein, J. Biol. Chem. 276 (2001) 45996–46003.
[23] C.W. Bertoncini, Y.-S. Jung, C.O. Fernandez, W. Hoyer, C. Griesinger, T.M. Jovin, M. Zweckstetter, Release of long-range tertiary interactions potentiates aggregation of natively unstructured α-synuclein, Proc. Natl. Acad. Sci. U. S. A. 102 (2005) 1430–1435.
[24] C.W. Bertoncini, C.O. Fernandez, C. Griesinger, T.M. Jovin, M. Zweckstetter, Familial mutants of α-synuclein with increased neurotoxicity have a destabilized conformation, J. Biol. Chem. 280 (2005) 30649–30652.
[25] Y.-H. Sung, D. Eliezer, Residual structure, backbone dynamics, and interactions within the synuclein family, J. Mol. Biol. 372 (2007) 689–707.

[26] K.-P. Wu, S. Kim, D.A. Fela, J. Baum, Characterization of conformational and dynamic properties of natively unfolded human and mouse α-synuclein ensembles by NMR: implication for aggregation, J. Mol. Biol. 378 (2008) 1104–1115.
[27] K.-P. Wu, D.S. Weinstock, C. Narayanan, R.M. Levy, J. Baum, Structural reorganization of α-synuclein at low pH observed by NMR and REMD simulations, J. Mol. Biol. 391 (2009) 784–796.
[28] L. Bousset, C. Brewee, R. Melki, F. Migliardo, Dynamical properties of α-synuclein in soluble and fibrillar forms by quasi elastic neutron scattering, Biochem. Biophys. Acta 1844 (2014) 1307–1316.
[29] S. Fujiwara, K. Araki, T. Matsuo, H. Yagi, T. Yamada, K. Shibata, H. Mochizuki, Dynamical behavior of human α-synuclein studied by quasielastic neutron scattering, PLoS One 11 (2016), e0151447.
[30] V.N. Uversky, J. Li, A.L. Fink, Metal-triggered structural transformations, aggregation, and fibrillation of human α-synuclein. A possible molecular link between Parkinson's disease and heavy metal exposure, J. Biol. Chem. 276 (2001) 44284–44296.
[31] L. Munishkina, J. Henriques, V.N. Uversky, A.L. Fink, Role of protein–water interactions and electrostatics in α-synuclein fibril formation, Biochemistry 43 (2004) 3289–3300.
[32] W. Hoyer, T. Antony, D. Cherny, G. Heim, T.M. Jovin, V. Subramaniam, Dependence of α-synuclein aggregate morphology on solution conditions, J. Mol. Biol. 322 (2002) 383–393.
[33] M.K. Jain, P. Singh, S. Roy, R. Bhat, Comparative analysis of the conformation, aggregation, interaction, and fibril morphologies of human α-, β-, γ-synuclein proteins, Biochemistry 57 (2018) 3830–3848.
[34] L. Bousset, L. Pieri, G. Ruiz-Arlandis, J. Gath, P.H. Jensen, B. Habenstein, K. Madiona, V. Olieric, A. Böckmann, B.H. Meier, R. Melki, Structural and functional characterization of two alpha-synuclein strains, Nature comm. 4 (2013) 1–13.
[35] A. Makky, L. Bousset, J. Polesel-Maris, R. Melki, Nanomechanical properties of distinct fibrillary polymorphs of the protein α-syuclein, Sci. Rep. 6 (37970) (2016).
[36] B. Winner, R. Jappelli, S.K. Maji, P.A. Desplats, L. Boyer, S. Aigner, C. Hetzer, T. Loher, M. Vilar, S. Campioni, C. Tzitzilonis, A. Soragni, S. Jessberger, H. Mira, A. Consiglio, E. Pham, E. Masliah, F.H. Gage, R. Riek, In vivo demonstration that α-synuclein oligomers are toxic, Proc. Natl. Acad. Sci. U. S. A. 108 (2011) 4194–4199.
[37] N. Cremades, S.I.A. Cohen, E. Deas, A.Y. Abramov, A.Y. Chen, A. Orte, M. Sandal, R.W. Clarke, P. Dunne, F.A. Aprile, C.W. Bertoncini, N.W. Wood, T.P.J. Knowles, C.M. Dobson, D. Klenerman, Direct observation of the interconversion of normal and toxic forms of α-synuclein, Cell 149 (2012) 1048–1059.
[38] E. Rockenstein, S. Nuber, C.R. Overk, K. Ubhi, M. Mante, C. Patrick, A. Adame, M. Trejo-Morales, J. Gerez, P. Picotti, P.H. Jensen, S. Campioni, R. Riek, J. Winkler, F.H. Gage, B. Winner, E. Masliah, Accumulation of oligomer-prone α-synuclein exacerbates synaptic and neuronal degeneration *in vivo*, Brain 137 (2014) 1496–1513.
[39] J.C. Smith, Protein dynamics: comparison of simulations with inelastic neutron scattering experiments, Q. Rev. Biophys. 24 (1991) 227–291.
[40] J. Pérez, J.M. Zanotti, D. Durand, Evolution of the internal dynamics of two globular proteins from dry powder to solution, Biophys. J. 77 (1999) 454–469.
[41] D.I. Svergun, M.H.J. Koch, P.A. Timmins, R.P. May, Small-Angle X-ray and Neutron Scattering from Solutions of Biological Macromolecules, Oxford university press, New York, 2013.
[42] H. Naiki, K. Higuchi, M. Hosokawa, T. Takeda, Fluorometric determination of amyloid fibrils in vitro using the fluorescent dye, thioflavin T1, Anal. Biochem. 177 (1989) 244–249.
[43] V.N. Uversky, J. Li, A.L. Fink, Evidence for a partially folded intermediate in α-synuclein fibril formation, J. Biol. Chem. 276 (2001) 10737–10744.
[44] J. Li, V.N. Uversky, A.L. Fink, Effect of familial Parkinson's disease point mutations A30P and A53T on the structural properties, aggregation, and fibrillation of human α-synuclein, Biochemistry 40 (2001) 11604–11613.
[45] A. Rekas, R.B. Knott, A. Sokolova, K.J. Barnham, K.A. Perez, C.L. Masters, S.C. Drew, R. Cappai, C.C. Curtain, C.L.L. Pham, The structure of dopamine induced α-synuclein oligomers, Eur. Biophys. J. 39 (2010) 1407–1419.
[46] D.I. Svergun, Determination of the regularization parameter in indirect-transform methods using perceptual criteria, J. Appl. Crystallogr. 25 (1992) 495–503.
[47] D. Franke, M.V. Petoukhov, P.V. Konarev, A. Panjkovich, A. Tuukkanen, H.D.T. Mertens, A.G. Kikhney, N.R. Hajizadeh, J.M. Franklin, C.M. Jeffries, D. Svergun, I. (2017) ATSAS 2.8: a comprehensive data analysis suite for small-angle scattering from macromolecular solutions, J. Appl. Crystallogr. 50 (2017) 1212–1225.
[48] G. Beaucage, Toward resolution of ambiguity for the unfolded state, Biophys. J. 95 (2008) 503–509.
[49] D. Franke, D.I. Svergun, DAMMIF, a program for rapid ab-initio shape determination in small-angle scattering, J. Appl. Crystallogr. 42 (2009) 342–346.
[50] V.V. Volkov, D.I. Svergun, Uniqueness of ab-initio shape determination in small-angle scattering, J. Appl. Crystallogr. 36 (2003) 860–864.
[51] M. Kozin, D.I. Svergun, Automated matching of high- and low-resolution structural models, J. Appl. Crystallogr. 34 (2001) 33–41.
[52] P. Bernadó, E. Mylonas, M.V. Petoukhov, M. Blackledge, D.I. Svergun, Structural characterization of flexible proteins using small-angle x-ray scattering, J. Am. Chem. Soc. 129 (2007) 5656–5664.
[53] G. Tria, H.D.T. Mertens, M. Kachala, D.I. Svergun, Advanced ensemble modelling of flexible macromolecules using x-ray solution scattering, IUCrJ 2 (2015) 207–217.
[54] M. Bée, Quasielastic Neutron Scattering, Adam Hilger, Bristol, U.K., and Philadelphia, U.S.A, 1988.
[55] A.M. Stadler, I. Digel, G.M. Artmann, J.P. Embs, G. Zaccai, G. Büldt, Hemoglobindynamics in red blood cells: correlation to body temperature, Biophys. J. 95 (2008) 5449–5461.
[56] F. Roosen-Runge, M. Henning, F. Zhang, R.M.J. Jacobs, M. Sztucki, H. Schrober, T. Seydel, F. Shreiber, Protein self-diffusion in crowded solutions, Proc. Natl. Acad. Sci. U. S. A. 108 (2011) 11815–11820.
[57] M. Monkenbusch, A. Stadler, R. Biehl, J. Ollivier, M. Zamponi, D. Richiter, Fast internal dynamics in alcohol dehydrogenase, J. Chem. Phys. 143 (2015), 075101.
[58] F. Ameseder, A. Radulescu, M. Khaneft, W. Lohstroh, A.M. Stadler, Homogeneous and heterogeneous dynamics in native and denatured bovine serum albumin, Phys. Chem. Chem. Phys. 20 (2018) 5128–5139.
[59] J.G. de la Torre, G. del Rio, A. Ortega, Improved calculation of rotational diffusion and intrinsic viscosity of bead models for macromolecules and nanoparticles, J. Phys. Chem. B 111 (2007) 955–961.
[60] A. Ortega, D. Amoros, J.G. de la Torre, Prediction of hydrodynamic and other solution properties of rigid proteins from atomic and residue-level models, Biophys. J. 101 (2011) 892–898.

[61] S. Fujiwara, T. Chatake, T. Matsuo, F. Kono, T. Tominaga, K. Shibata, A. Sato-Tomita, N. Shibayama, Ligation-dependent picosecond dynamics in human hemoglobin as revealed by quasielastic neutron scattering, J. Phys. Chem. B 121 (2017) 8069–8077.
[62] T. Matsuo, T. Tominaga, F. Kono, K. Shibata, S. Fujiwara, Modulation of the picosecond dynamics of troponin by the cardiomyopathy-causing mutation K247R of troponin T by quasielastic neutron scattering, BBA – Proteins and Proteomics 1865 (2017) 1781–1789.
[63] F. Ameseder, A. Radulescu, O. Holderer, P. Falus, D. Richter, A.M. Stadler, Relevance of internal friction and structural constraints for the dynamics of denatured bovine serum albumin, J. Phys. Chem. Lett. 9 (2018) 2469–2473.
[64] F. Volino, A.J. Dianoux, Neutron incoherent-scattering law for diffusion in a potential of spherical symmetry: general formalism and application to diffusion inside a sphere, Mol. Phys. 41 (1980) 271–279.
[65] M.-K. Cho, G. Nodet, H.-Y. Kim, M.R. Jensen, P. Bernado, C.O. Fernandez, S. Becker, M. Blackledge, M. Zweckstetter, Structural characterization of α-synuclein in an aggregation prone state, Protein Sci. 18 (2009) 1840–1846.
[66] J.C. Lee, R. Langen, P.A. Hummel, H.B. Gray, J.R. Winkler, α-Synuclein structures from fluorescence energy-transfer kinetics: Implications for the role of protein in Parkinson's disease, Proc. Natl. Acad. Sci. U. S. A. 101 (2004) 16466–16471.
[67] A.J. Trexler, E. Rhodes, Single molecule characterization of α-synuclein in aggregation-prone states, Biophys. J. 99 (2010) 30248–33055.
[68] J. Bai, K. Cheng, M. Liu, C. Li, Impact of the α-synuclein initial ensemble structure on fibrillation pathways and kinetics, J. Phys. Chem. B 120 (2016) 3140–3147.
[69] H. Yagi, E. Kusaka, K. Hongo, T. Mizobata, Y. Kawata, Amyloid fibril formation of α-synuclein is accelerated by preformed amyloid seeds of other proteins. Implications for the mechanism of transmissible conformational diseases, J. Biol. Chem. 280 (2005) 38609–38616.
[70] L. Narhi, S.J. Wood, S. Steavenson, Y. Jiang, G.M. Wu, D. Anafi, S.A. Kaufman, F. Martin, K. Sitney, P. Denis, J.-C. Louis, J. Wypych, A.L. Biere, M. Citron, Both familial Parkinson's disease mutations accelerate α-synuclein aggregation, J. Biol. Chem. 274 (1999) 9842–9846.
[71] A. Guinier, G. Fournet, Small-Angle Scattering of x-rays, John Wiley and Sons, Inc, New York, 1955.
[72] S.W. Provencher, A constrained regularization method for inverting data represented by linear algebraic or integral equations, Comp. Phys. Comm. 27 (1982) 213–227.
[73] K. Shibata, N. Takahashi, Y. Kawakita, M. Matsuura, T. Yamada, T. Tominaga, W. Kambara, M. Kobayashi, Y. Inamura, T. Nakatani, K. Nakajima, M. Arai, The performance of TOF near backscattering spectrometer DNA in MLF, J-PARC, JPS Conf. Proc. 8 (2015), 036022.
[74] A.M. Gasper, S. Busch, M.-S. Appavou, W. Haeussler, R. Georgii, Y. Su, W. Doster, Using polarization analysis to separate the coherent and incoherent scattering from protein samples, Biochem. Biophys. Acta. 2804 (2010) 76–82.
[75] L. Rusevich, J. Embs, H. Paulsen, G. Renger, J. Pieper, Protein and solvent dynamics of the water-soluble chlorophyll-binding protein (WSCP), EPJ Web Conf. 83 (2016), 02016.
[76] S. Fujiwara, T. Yamada, T. Matsuo, N. Takahashi, K. Kamazawa, Y. Kawakita, K. Shibata, Internal dynamics of a protein that forms the amyloid fibrils observed by neutron scattering, J. Phys. Soc. Jpn. 82 (2013) SA019.